Environmental Science and Ecotechnology 13 (2023) 100219

Contents lists available at ScienceDirect

Environmental Science and Ecotechnology

journal homepage: www.journals.elsevier.com/environmental-science-and-ecotechnology/

Original Research

Ceftriaxone sodium degradation by carbon quantum dots (CQDs)-decorated C-doped α-Bi_2O_3 nanorods

Xianbo Sun [a], Ying Pan [a], Yanyu Song [a], Wen Liu [b], Long D. Nghiem [c], Qilin Wang [c], Zhengqing Cai [a, d, *]

[a] National Engineering Research Center of Industrial Wastewater Detoxication and Resource Recovery, East China University of Science and Technology, Shanghai, 200237, China
[b] The Key Laboratory of Water and Sediment Sciences, Ministry of Education, College of Environmental Sciences and Engineering, Peking University, Beijing, 100871, China
[c] Centre for Technology in Water and Wastewater, School of Civil and Environmental Engineering, University of Technology Sydney, Ultimo, NSW, 2007, Australia
[d] Shanghai Institute of Pollution Control and Ecological Security, Shanghai, 200237, China

ARTICLE INFO

Article history:
Received 13 July 2022
Received in revised form
1 November 2022
Accepted 1 November 2022

Keywords:
Photocatalytic
Antibiotics
C-doped
Carbon quantum dots
Toxicity assessment

ABSTRACT

A novel carbon quantum dots decorated C-doped α-Bi_2O_3 photocatalyst (CBO/CQDs) was synthesized by solvothermal method. The synergistic effect of adsorption and photocatalysis highly improved contaminants removal efficiencies. The ceftriaxone sodium degradation rate constant (k) of CBO/CQDs was 11.4 and 3.2 times that of pure α-Bi_2O_3 and C-doped α-Bi_2O_3, respectively. The interstitial carbon doping generated localized states above the valence band, which enhanced the utilization of visible light and facilitated the separation of photogenerated electrons and holes; the loading of CQDs improved the charge carrier separation and extended the visible light response; the reduced particle size of CBO/CQDs accelerated the migration of photogenerated carriers. The $\bullet O_2^-$ and h^+ were identified as the dominant reactive species in ceftriaxone sodium degradation, and the key role of $\bullet O_2^-$ was further investigated by NBT transformation experiments. The Fukui index was applied to ascertain the molecular bonds of ceftriaxone sodium susceptible to radical attack, and intermediates analysis was conducted to explore the possible degradation pathways. The toxicity evaluation revealed that some degradation intermediates possessed high toxicity, thus the contaminants require sufficient mineralization to ensure safe discharge. The present study makes new insights into synchronous carbon dopping and CQDs decoration on modification of α-Bi_2O_3, which provides references for future studies.

1. Introduction

Antibiotics have been extensively used to prevent and treat human bacterial infections and animal husbandry since the discovery of penicillin in 1929 [1]. Recent studies showed that the total usage of 36 antibiotics in China was 92 700 tons in 2013, of which human and animal excreted around 54 000 tons; part of them entered the environment due to insufficient removal by conventional wastewater treatment [2]. Moreover, the manufacturing processes, landfill leachates, agricultural and animal feeding operations, and urban run-off also released large amount of antibiotics to the environment [3,4]. The residual antibiotics are frequently detected in the level of $ng \cdot L^{-1}$ to $\mu g \cdot L^{-1}$ in the environment and even in drinking water [5,6]. Antibiotics have been reported to exhibit chronic toxicity to invertebrates and fish. Moreover, they promote the development of antibiotic-resistant bacteria, thus causing a potential threat to human health [7–9]. Therefore, it is important to develop effective methods to eliminate antibiotics in water.

The semiconductor photocatalysis has attracted considerable attention in organic pollutants removal owing to its economic and environmentally friendly characteristics [10–12]. Among various materials, the bismuth oxide (Bi_2O_3) is considered a promising

* Corresponding author. National Engineering Research Center of Industrial Wastewater Detoxication and Resource Recovery, East China University of Science and Technology, Shanghai, 200237, China.
E-mail address: caizhengqing@ecust.edu.cn (Z. Cai).

https://doi.org/10.1016/j.ese.2022.100219

photocatalyst because of its narrow band gap, nontoxicity, and high dielectric permittivity [13,14]. Bi_2O_3 has six crystalline forms, two stable phases (α-Bi_2O_3 and δ-Bi_2O_3) and four metastable phases (β-Bi_2O_3, γ-Bi_2O_3, ε-Bi_2O_3 and ω-Bi_2O_3). The stable phase α-Bi_2O_3 has been the most researched because of its high thermal stability, environmentally benign characteristics, and narrow band gap (E_g = 2.80 eV), thereby showing high potential for photocatalytic degradation of contaminants [15,16]. However, most reported Bi_2O_3 are bulk materials with limited visible light activity and rapid charge carriers recombination, thus showing relatively low photocatalytic activity [17–19].

Researchers have applied various strategies to extend the light utilization of α-Bi_2O_3 and boost its charge carriers separation and transfer efficiency, such as element doping [20,21], surface modification [22], morphology control [23] and heterostructure construction [24,25]. Among these methods, carbon doping introduces exogenous ions in the α-Bi_2O_3 lattice, broadening its visible light absorption and causes higher photocatalytic activity. For instance, a carbon doped porous Bi_2O_3 synthesized by using glycol as carbon source, showed obvious red-shift on its absorption edge and improved photocatalytic activity on contaminants degradation [26]. However, the C-doped Bi_2O_3 still exhibits poor electron-hole separation, restraining its application. Glucose is another widely used carbon precursor for carbon doping of semiconductors such as C-doped TiO_2 [27], C-doped $(BiO)_2CO_3$ [28], and C-doped BiOI [29], all of which showed elevated photocatalytic activity owing to the extended visible light utilization or charge separation.

Carbon quantum dots (CQDs), a new class of "zero-dimensional" nanostructures, have excellent up-converted photoluminescence, photoinduced electron transfer, and electron reservoir properties [30,31]. The CQDs could transfer the near infrared or infrared light into ultraviolet and visible light, thus enabling the CQDs/Bi_2O_3 to utilize light with longer wavelength. Moreover, the CQDs decorated Bi_2O_3 also showed accelerated separation of photogenerated electron-hole pairs [32,33]. Therefore, combining CQDs modification and carbon doping can be an effective method to construct a highly active Bi_2O_3-based photocatalyst. Understanding the synergistic effects between these two carbon modification methods can be significant.

In this work, we synthesized a C-doped α-Bi_2O_3 with CQDs decoration (CBO/CQDs) by using glucose as carbon source. The retarded electron-hole recombination and extended visible light absorbance of the new material were revealed by photodegradation of ceftriaxone sodium (a typical antibiotic) and various material characterization techniques. Morever, the possible photocatalytic degradation mechanism and pathways of ceftriaxone sodium were proposed by radical quenching experiments, intermediates analysis, and density functional theory (DFT) calculation. The toxicity evolution of ceftriaxone sodium in the degradation process was revealed by quantitative structure-activity relationship (QSAR) prediction. This study makes new insights into synchronous carbon doping and CQDs deposition on α-Bi_2O_3, thus, providing a base for future studies.

2. Material and methods

2.1. Synthesis of α-B_2O_3 and carbon doped α-B_2O_3

Carbon doped α-B_2O_3 (CBO) was prepared by hydrothermal and post-calcination method [34]. Briefly, 8 mmol of $Bi(NO_3)_3{\cdot}5H_2O$ and a designated amount of glucose were mixed and grounded by agate mortar for 15 min. The obtained powder was added into the solution with 160 mL of deionized water and 4 mL of concentrated nitric acid, and sonicated to reach complete dissolution. The pH was adjusted to 12.6 by NaOH under strong agitation, and a yellow suspension was formed. The mixture was vigorously stirred for another 30 min, and the suspension was added in a 250 mL autoclave and heated at 160 °C for 24 h. After the reaction, the precipitate was collected and washed three times with ethanol and ultrapure water, then dried overnight at 60 °C. The obtained deep gray product was milled into powder, and calcined in a muffle furnace at 450 °C for 6 h (with a temperature raising rate of 5 °C min^{-1}). The deep gray powder turned yellow due to carbon removal on the surface layer. For simplicity, the materials were named as CBO-*x* (*x* = 2, 3, 4), where x refers to the mole ratio of glucose to $Bi(NO_3)_3{\cdot}5H_2O$. For comparison, pristine α-Bi_2O_3 (BO) was synthesized by the same method but without adding glucose.

2.2. Synthesis of C- doped α-B_2O_3/CQDs

CQDs were synthesized by using secondary solvothermal treatment with ethylene glycol (EG), which reduced part of the doped carbon and exfoliated the material [35]. Specifically, the CQDs decorated C-doped α-B_2O_3 (CBO/CQDs) was synthesized through solvothermal treatment of CBO-x (as shown in Scheme 1). The used procedure was as follows: 1.1878 g of CBO-x photocatalyst was dispersed in 80 mL of EG and kept stiring for 1 h; the suspension was then transferred into a 150 mL autoclave and maintained at 160 °C for 12 h; after the reaction, the resulting precipitate was washed with ethanol and ultrapure water three times; finally, the obtained CBO/CQDs was freeze dryed under vacuum. The EG exploited α-Bi_2O_3 (BO/EG) was prepared by treating pristine α-Bi_2O_3 by the same method.

The as-prepared materials information is shown in Text S1-2 of the Supporting Information (SI).

2.3. Photocatalytic experiments

The photocatalytic performance of synthesized catalysts was investigated *via* degrading ceftriaxone sodium under simulated sunlight by using a 300 W Xenon lamp (Perfect Light, PLS-SXE 300, Beijing, China). The used procedure was as follows: 0.015g of catalyst was added into a ceftriaxone sodium solution (250 mL, 10 mg L^{-1}) and kept stirring in the dark for 60 min to achieve adsorption-desorption equilibrium; the suspension was transferred to a photo-reactor with cooling system and exposed to simulated solar light; at predetermined irradiation time intervals, 2 mL of suspension was withdrawn and filtered through a 0.22 μm nylon syringe filter for analysis. The visible-light activity of catalysts were evaluated by applying a 420 nm cutoff filter to shield the UV portion of solar light.

The ceftriaxone sodium degradation data fitted a pseudo-first-order kinetic law expressed by equation (1) [36]:

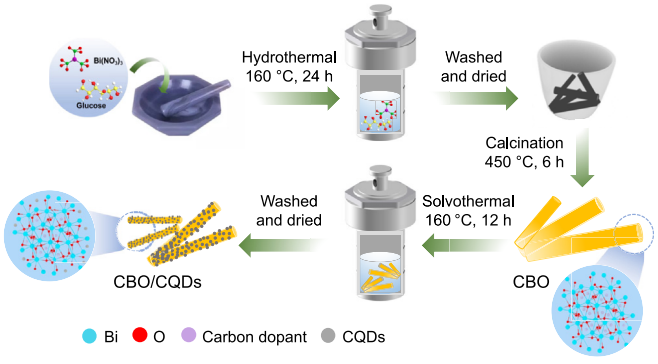

Scheme 1. The preparation of CBO/CQDs photocatalyst.

$$-\ln\left(\frac{C_t}{C_0}\right) = kt \quad (1)$$

where C_0 and C_t are the initial and final pollutant concentrations after t minutes of illumination, respectively, and k is the pseudo-first-order rate constant (min^{-1}).

To evaluate the stability of the CBO/CQDs photocatalyst, the degradation of ceftriaxone sodium was repeated four times under identical conditions. Before every reuse cycle the photocatalyst was collected by membrane filtration, washed with dionized water, and dried at 60 °C.

2.4. Detection of reactive oxygen species

To identify the reactive species produced in the photocatalysis process with CBO/CQDs, various trapping agents; ammonium oxalate (AO, 700 mg L^{-1}), p-benzoquinone (BQ, 80 mg L^{-1}), tert-butanol (TBA, 10 mmol L^{-1}), and L-histidine (L-his, 1 mmol L^{-1}) were utilized to trap photogenerated holes (h^+), superoxide radicals ($\bullet O_2^-$), hydroxyl radicals ($\bullet OH$), and $^1O_2$, respectively.

The amount of $\bullet O_2^-$ generated from the photocatalysis process was further analyzed by nitroblue tetrazolium (NBT) transformation experiments, where the ceftriaxone sodium was replaced by NBT (20 μM) in the experiments, using an identical procedure to the aforementioned photocatalytic degradation experiment. NBT reacted with $\bullet O_2^-$ at the molar ratio of 1: 4 to generate formazan precipitate with an absorption peak at 680 nm, which resulted in the decrease of the characteristic absorbance peak of NBT (at 259 nm) [37,38].

2.5. Analytical methods, DFT calculation, and toxicity evaluation

The detailed analytical methods of ceftriaxone sodium and degradation intermediates, as well as their toxicity evaluation method, are presented in Text S3. The density functional theory (DFT) calculation based on Fukui function was applied to ascertain the attacked sites of ceftriaxone sodium. These results were applied to interpret the photocatalytic degradation mechanism (Text S4).

3. Results and discussion

3.1. Morphology and structural characteristics

The microstructures of pure BO, CBO-3, and CBO/CQDs were characterized by field emission scanning electron microscopy (FESEM). As shown in Fig. 1a, the BO sample synthesized by hydrothermal and post-calcination method consists of microcrystals with rod-like structures. During the hydrothermal synthesis of CBO-3, the glucose adsorbed on the surface of the precursor may have prevented the growth of rod structure. With the increase of hydrothermal time, the rodlets gradually grew in different directions thus forming an irregular porous rod-shaped stacking structure (Fig. 1b). It can be observed that the introduction of external carbon significantly affected the rod structure of BO. As shown in Fig. 1c, the irregular porous rod-shaped stacking structure was further reduced to a rod-like structure with slit-like pores when the CBO-3 was solvothermally treated with EG. Obviously, the diameter and length of CBO/CQDs were smaller than pure BO. The particle size reduction provided more surface-active sites, favouring contaminants' adsorption and hence improved the photocatalytic performance of CBO/CQDs.

More detailed micromorphology and microstructure of CBO/CQDs were further characterized by transmission electron microscope (TEM). In Fig. 1d, the CBO/CQDs shows a rod-like structure with slit-like pores and some nanosheets on the surface, which is in accordance with the FESEM results. Meanwhile, a large number of CQDs with diameters of 3–9 nm are spread over the nanosheets and rod-like structure (Fig. 1e and g). Fig. 1f shows the high-resolution TEM (HRTEM) image of CBO/CQDs; the lattice fringes with an interplanar space of 0.28 nm coincide with (012) the plane of α-Bi_2O_3 crystal, which is consistent with the X-ray powder diffraction (XRD) results. The clear lattice fringes distances of 0.21 nm and 0.24 nm were observed in CBO/CQDs, which correspond to the (100) and (102) in-plane lattice of CQDs [39,40]. Furthermore, the elemental composition and distribution of CBO/CQDs were evaluated by elemental mapping (Fig. 1h), which shows that the Bi, O, and C are homogeneously distributed; these results further confirm the successful synthesis of CBO/CQDs photocatalyst.

The crystalline structures of bare BO, CBO-3, and CBO/CQDs were characterized using XRD, as shown in Fig. 2a. The strong diffraction peaks of pure BO are identified at 25.8°, 26.9°, 27.4°, 28.0°, 33.0°, 27.4°, 33.2°, 46.3°, and 52.4°, which are ascribed to the (002), (111), (120), (012), (121), (200), (041), and (−321) crystal planes for bulk α-Bi_2O_3 with monoclinic structure (JCPDS Card No. 41-1449) [17]. After doping with carbon and modified by CQDs, no diffraction peaks other than α-Bi_2O_3 were found. This is likely caused by the low dosage of doped carbon and CQDs, as well as the high dispersion of CQDs on the BO surfaces. This is consistent with the TEM analysis. The peaks intensities of CBO-3 and CBO/CQDs decrease when compared with BO, indicating that the CBO-3 and CBO/CQDs maintain the crystal structure as pure BO, but carbon doping can influence the crystal growth [28], which is in agreement with the FESEM analysis. The amplified XRD pattern reveals that the crystal peak (120) of CBO-3 and CBO/CQDs shows a slight peak shift in the 2θ range of 27°–28°, suggesting that some carbon atoms were successfully doped into the lattice of BO crystal [41].

In Fig. 2b, the Raman spectra of BO, CBO-3 and CBO/CQDs are almost the same, all the peaks agree well with monoclinic α-Bi_2O_3. The peaks at 105, 120, 138, 153, 184, 212, 282, 313, and 449 cm^{-1} are consistent with the values reported for α-Bi_2O_3 [42,43]. However, no signal was observed for doped carbon and CQDs in Raman spectrum, which can be explained by their low dosage.

The N_2 adsorption-desorption isotherms and pore size distribution of BO, CBO-3, and CBO/CQDs are shown in the Fig. 2c–f, and the detailed specific surface, pore volume and pore size distributions are listed in Table S1. The CBO/CQDs exhibits the largest surface area (~30.9 m^2 g^{-1}) and pore volume (~0.08 cm^3 g^{-1}). Normally, samples with large specific areas show superior photocatalytic activity because of their higher number of adsorption sites and active centers [44]. This agrees with the results of photodegradation experiments. According to IUPAC, CBO-3 and CBO/CQDs have classical type IV adsorption-desorption isotherm with H3 hysteresis loops, which indicates the prevalence of mesoporous structures or slit-like pores or both [45]. Moreover, the pore sizes of CBO-3 and CBO/CQDs are mainly 20–30 nm and 1–5 nm, demonstrating that CBO-3 is mesoporous. Meanwhile, both the FESEM and TEM analysis reveal the presence of slit-like pores in CBO/CQDs. However, the pure BO shows the smallest surface area (~0.8 m^2 g^{-1}), it has type III adsorption-desorption isotherm with nearly no hysteresis loops, indicating the presence of exterior macropores between stacked rods. This can partially explain the poor photocatalytic activity of the synthesized pristine α-Bi_2O_3. It should be noted that the adsorption and desorption isotherms of BO and CBO-3 do not coincide at low relative pressure, which may be explained by the low specific surface area of these two materials.

The X-ray photoelectron spectroscopy (XPS) was employed to analyze the surface elemental compositions and valence states of CBO/CQDs (shown in Fig. 3). The full-survey XPS spectra show that

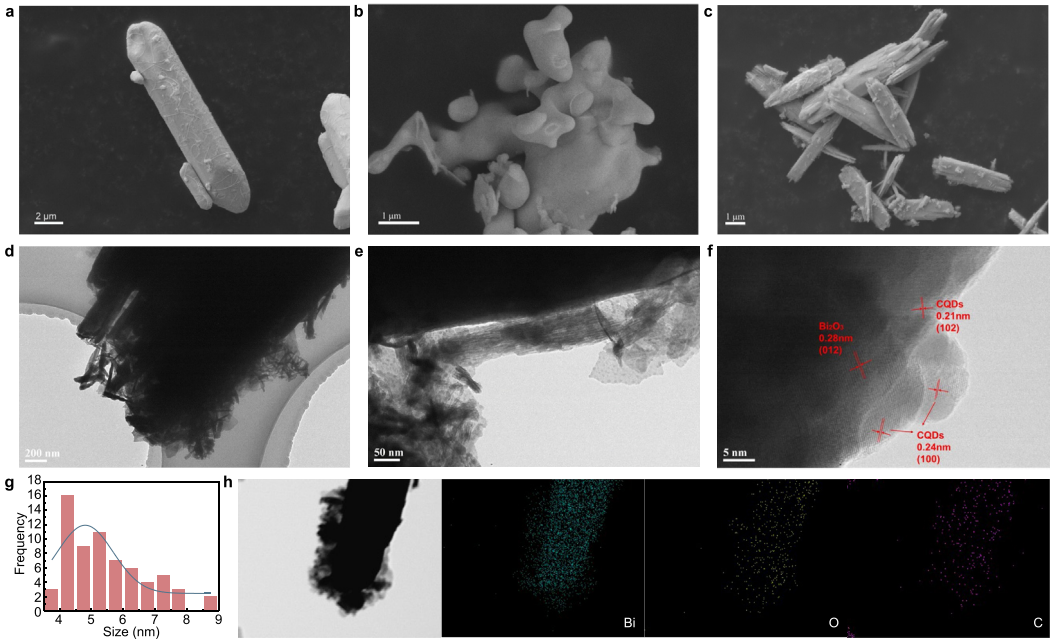

Fig. 1. **a**–**c**, FESEM images of BO (**a**), CBO-3 (**b**), CBO/CQDs (**c**). **d**–**e**, TEM images of CBO/CQDs. **f**, HRTEM image of CBO/CQDs. **g**, Particle size distribution of CQDs. **h**, TEM image of CBO/CQDs and the corresponding elemental mapping analysis for Bi, O, and C.

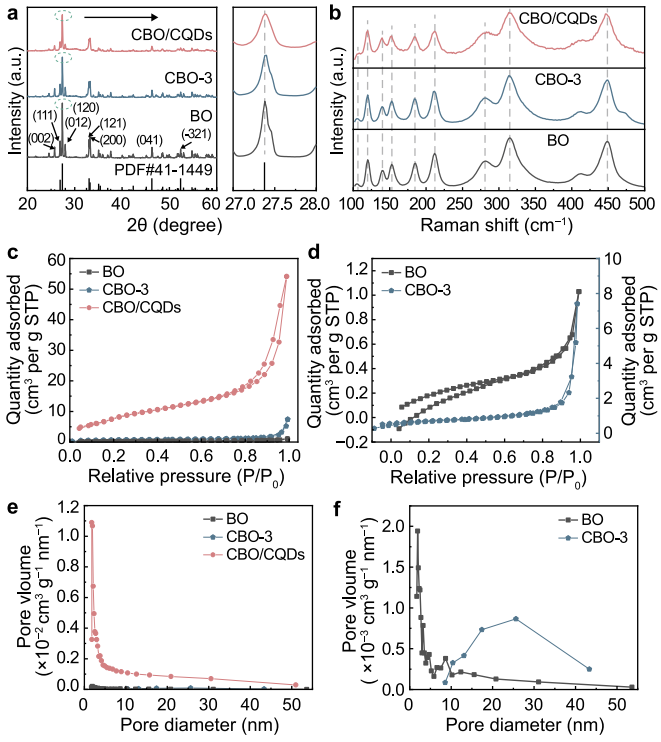

Fig. 2. **a**–**b,** XRD patterns (**a**) and Raman spectra (**b**) of BO, CBO-3, and CBO/CQDs. **c**–**d**, Nitrogen adsorption–desorption isotherms of BO, CBO-3, and CBO/CQDs (**c**)**, and** of BO and CBO-3 with more details (**d**). **e**–**f**, Pore size distribution of BO, CBO-3, and CBO/CQDs (**e**), and of BO and CBO-3 with more details (**f**).

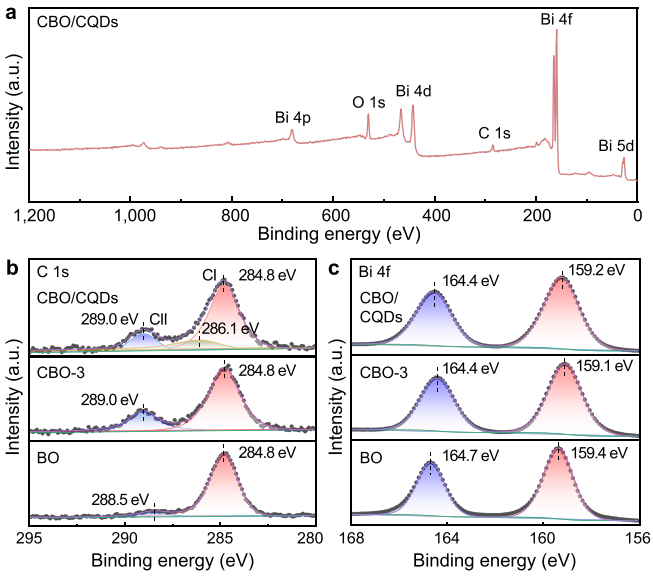

Fig. 3. The XPS spectra: **a**, survey spectrum of CBO/CQDs; **b**, C 1s of BO, CBO-3, and CBO/CQDs; **c**, Bi 4f of BO, CBO-3, and CBO/CQDs.

the CBO/CQDs photocatalyst is composed of Bi, O, and C (Fig. 3a). Fig. 3b shows the C1s XPS spectra of BO, CBO-3, and CBO/CQDs. Two C1s peaks are observed at 284.8 eV (CI) and 288.5 eV in the XPS spectrum of BO, which can be due to the adventitious carbon from the instrument and absorbed CO_2 [46]. For CBO-3 and CBO/CQDs, the C1s peak at 289.0 eV (CII) indicates the presence of carbonate species (C═O and/or O–C═O) [28,47]. No carbon peak is observed at 281 eV, suggesting that either there is no Bi–C bond, or it is too weak to be observed in the C-doped samples [26,48]. These observations indicate that the doped carbon does not substitute the lattice oxygen in BO; it eventually leads doped carbon to stay in the interlayer of BO *via* interstitial doping [49,50]. The new carbon peak of CBO/CQDs at 286.1 eV is attributed to the oxygenated carbon, suggesting the presence of CQDs on the surface [51]. This fact is consistent with the HRTEM results. The content of carbon doping (atom ratio) in CBO-3 and CBO/CQDs can be estimated by the XPS

measurement. As shown in Table S2, the carbon content in CBO-3 and CBO/CQDs is 7.42% and 4.05% respectively, indirectly prove that secondary EG solvothermal reduced part of doping carbon to CQDs. The Bi 4f spectra of pure BO sample (Fig. 3c) has two characteristic XPS peaks of Bi^{3+}, which are ascribed to Bi^{3+} $4f_{5/2}$ and Bi^{3+} $4f_{7/2}$, respectively [52]. The Bi 4f peaks of CBO-3 and CBO/CQDs slightly shift to lower binding energy after the addition of glucose, this result is consistent with C-doped In_2O_3 [53], further proofs the successful carbon doping in BO. Therefore, based on XRD, HRTEM, and XPS results, the doped carbon and CQDs are presented in the interlayer and surface of BO.

3.2. The optical absorption properties and band structure of materials

The UV–vis diffuse reflectance spectroscopy (UV–vis DRS) was used to study the optical properties of the obtained materials. In Fig. 4a, the light absorption edge of bare BO is at 457 nm. With the carbon doping, the absorption of the C-doped BO exhibits obvious red-shift, where the absorption edge of CBO-3 and CBO/CQDs are located at 515 and 479 nm, respectively. This is because the doped carbon in the lattice of the BO introduces localized states near the top of the VB and thus enhances the intrinsic optical absorption of BO [50,54]. Meanwhile, the light absorption intensity at 450–800 nm is significantly increased for CBO/CQDs with the loading of CQDs (as photosensitizer), indicating enhanced light absorption. Therefore, CQDs and C-doping play important roles in enhancing the visible light absorption of the CBO/CQDs, which is expected to enhance its photocatalytic activity.

In general, the band gap energy (E_g) of a semiconductor photocatalyst can be calculated *via* the Kubelka-Munk equation (equation (2)):

$$\alpha h\nu = A(h\nu - E_g)^{\frac{n}{2}} \quad (2)$$

where α, $h\nu$, E_g, and A are the absorption coefficient, photon energy, band gap, and Planck's constant, respectively.

The E_g of the BO, CBO-3, and CBO/CQDs are determined from a plot of $(\alpha h\nu)^{1/2}$ versus $h\nu$ [55,56]. Therefore, the E_g of BO, CBO-3, and CBO/CQDs are calculated as 2.73, 2.39, and 2.60 eV, respectively. There results indicate that the C doping in the crystal structure narrows the E_g of BO, improving photocatalytic activity.

The Mott-Schottky plots were performed to analyze the flat-band potentials (E_{fb}) and semiconductivity type of the synthesized materials. The E_{fb} of BO, CBO-3, and CBO/CQDs are −0.42, 0.40, and −0.39 eV vs. NHE, respectively (Fig. 4b–c and Fig. S1). Moreover, the positive slope of the Mott-Schottky curves of as-prepared photocatalysts indicate that they are all n-type semiconductors [57]. In general, the conduction band (CB) potential of n-type semiconductors is known to locate 0.2 eV more negative relative to the E_{fb} potential of the material [58]. Therefore, the E_{CB} of BO, CBO-3, and CBO/CQDs are estimated to be −0.62, 0.60, and −0.59 eV, respectively. The valence band (VB) positions of BO, CBO-3, and CBO/CQDs are calculated *via* the equation of $E_{VB} = E_{CB} + E_g$. Therefore, the E_{VB} of BO, CBO-3, and CBO/CQDs are calculated as 2.11, 1.79, and 2.01 eV, respectively. These results are close to the E_{VB} estimated by XPS VB spectra (as 2.09, 1.76, and 1.97 eV in Fig. S2). The results indicate that the interstitial carbon mainly changes the VB of BO. Similar results have been reported in the interstitial C doped BiOI and C doped Bi_3O_4Cl [29,34]. The carbon atoms located at interstitial positions of Bi_2O_3 lead to lattice distortion and the formation of occupied states within the gap, which decrease the band gap. The higher doping concentration induces a greater distortion degree, resulting in lower band gap [59,60]. With the increase of doped carbon dosage, the band-gap energies and VB of the materials will decrease accordingly. This explains why the E_g and VB of CBO/CQDs are higher than CBO-3.

The photoluminescence (PL) spectra of various materials were investigated to reveal the recombination rate of photogenerated electron-hole pairs (as shown in Fig. 4d). The pure BO shows the highest peak intensity, suggesting that it suffered from high electron and hole recombination. This might be the primary reason for the poor photocatalytic activity of BO on ceftriaxone sodium degradation. The CBO-3 and CBO/CQDs exhibit similar PL spectra as pure BO, while the PL emission peak intensity of CBO-3 decreases, indicating that the carbon doping reduces the recombination efficiency of photogenerated carriers. Meanwhile, CBO/CQDs exhibits the lowest PL intensity, suggesting that it has the best photogenerated carrier separation performance, mainly caused by the cooperative contribution of carbon doping and CQDs. The photocurrent (PC) response was used to study the separation of photogenerated carriers; the stronger the photocurrent intensity the higher the separation efficiency of photogenerated carriers [61]. In Fig. 4e, the CBO/CQDs shows the strongest PC intensity, indicating that it possesses an enhanced photon-generated carriers separation efficiency. Meanwhile, the intensity value of CBO-3 is stronger than that of pure BO, which shows that the doped carbon enhances the electrons-holes separation.

Additionally, electrochemical impedance spectra (EIS) Nyquist plots were obtained to study the interfacial charge transfer property of as-prepared catalysts [62]. Generally, the smaller arc radius indicate lower impedance and higher charge transfer efficiency [63]. As shown in Fig. 4f, the radius of the EIS Nyquist plots are in the following order: BO > CBO-3 > CBO/CQDs; CBO/CQDs exhibits

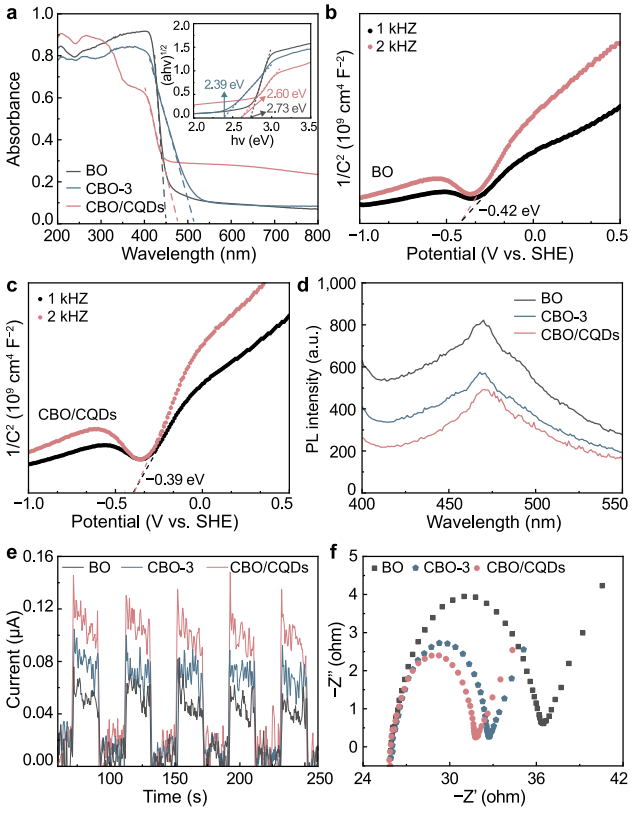

Fig. 4. **a**, UV–vis DRS of BO, CBO-3, and CBO/CQDs, the inset shows their Tauc plots. **b**–**c**, Mott-Schottky plots of BO (**b**) and CBO/CQDs (**c**). **d**–**f**, PL spectra (**d**), PC spectra (**e**), and EIS Nyquist (**f**) plots of BO, CBO-3, and CBO/CQDs.

the smallest arc radius among those samples, showing its minimum carrier transport resistance and fastest interfacial charge transfer, which is probably caused by the synergistic effects of carbon doping, introduction of CQDs, and reduced particle size. The results of PL spectra, photocurrent and EIS demonstrate that the CBO/CQDs has low electron-hole recombination and high separation and transfer capability. Thus, the CBO/CQDs is supposed to exhibit higher photocatalytic activity on contaminants degradation.

3.3. Photocatalytic performance of synthesized materials on ceftriaxone sodium degradation

To evaluate the photocatalytic activities of BO, CBO, BO/EG, and CBO/CQDs, the photodegradation of ceftriaxone sodium was performed under simulated sunlight irradiation. All the photocatalysts were kept stirring in the dark for 60 min to reach the adsorption-desorption equilibrium before photocatalysis. As shown in Fig. S3, adsorption efficiency of ceftriaxone sodium by BO and CBO is low (<4%), while CBO/CQDs shows increased adsorption efficiency (22.3%). This may be primarily caused by the increased surface-active sites of the synthesized CBO/CQDs, as revealed by FESEM and BET analysis (Figs. 1 and 2). According to the control experiment, the photodegradation of ceftriaxone sodium can be negligible (Fig. 5a), showing its high stability under sunlight. The carbon doping enhanced the photocatalytic activity of the pure BO; however, further increasing the carbon content decreases its photocatalytic activity. Higher carbon doping content may form more defect sites in the α-Bi_2O_3 lattice, acting as recombination centers [28]. This suggests that proper carbon doping content can efficiently improve the degradation efficiency. The *k* value of CBO-3 (0.0064 min^{-1}) is 3.55 times that of pure BO (Fig. 5c), showing its improved photocatalytic activity. The introduction of carbon in the interlayer of BO leads to the adjustment of energy band structures, which further expands the absorption range of visible light and separation efficiency of photo-generated carriers. Therefore, the CBO-3 was chosen as the precursor for synthesizing CBO/CQDs.

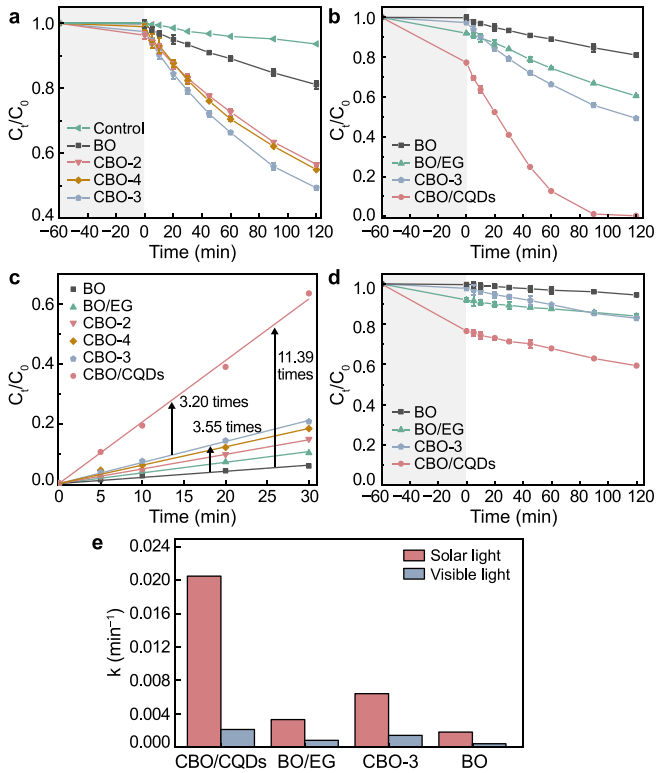

Fig. 5. **a**–**b**, Photocatalytic degradation of ceftriaxone sodium under simulated sunlight by the CBO-*x* (**a**), and by BO, BO/EG, CBO-3, and CBO/CQDs (**b**). **c**, The linear plot of $ln(C_0/C_t)$ versus *t* of different catalysts under solar light. **d**, Photocatalytic degradation kinetics of ceftriaxone sodium under visible light by BO, BO/EG, CBO-3, and CBO/CQDs. **e**, The first order kinetic constant (*k*) of ceftriaxone sodium degradation under solar light and visible light by BO, BO/EG, CBO-3, and CBO/CQDs.

Fig. 5b shows the photocatalytic ceftriaxone sodium degradation efficiency of BO, CBO-3, BO/EG, and CBO/CQDs, reaching 18.9%, 50.7%, 39.4%, and 99.7%, respectively, under simulated sunlight irradiation within 120 min. Besides, the UV–vis and HPLC spectra of ceftriaxone sodium are weakening with time (Fig. S4), indicating the decomposition of ceftriaxone sodium. As shown in Fig. 5c, the reaction constant *k* of CBO/CQDs (0.0205 min^{-1}) is 11.39 times that of pure BO and 3.20 times that of CBO-3. The presence of CQDs can effectively enhance the light absorption and the photo-generated holes-electrons separation, thus greatly increasing the photocatalytic activity. This is also supported by the UV–vis spectra, PL, photocurrent response, and EIS test. Several studies have investigated the photocatalytic degradation of ceftriaxone sodium (as shown in Table S3), but the applied catalysts dosage (0.5–7.0 g L^{-1}) is much higher than in this study (0.06 g L^{-1}), and their obtained *k* values are in the range of 0.0026–0.0249 min^{-1}, which is equal or lower to the *k* value (0.0205 min^{-1}) in this study. Therefore, the synthesized photocatalyst in our work has excellent photocatalytic degradation efficiency on ceftriaxone sodium compared with the photocatalysts reported in other studies.

To reveal the improved visible light utilization efficiency of CBO/CQDs, its photocatalytic performance under visible and solar light were compared (Fig. 5d). Fig. 5e shows that the *k* value in the presence of CBO/CQDs and CBO-3 are 5.25 and 3.50 times that of pure BO under visible light. The previous UV–vis absorption spectra of the catalysts (Fig. 4a) showed the enhanced visible light absorption by CBO/CQDs and CBO-3, which can well elucidate the improved visible light photocatalytic performance. The up-conversion fluorescent properties of CQDs could enlarge the light responsive range, and the photocatalytic efficiency of CBO/CQDs under visible light was further improved [64]. The *k* value of photocatalysts under visible light follow the order: BO < BO/EG < CBO-3 < CBO/CQDs, which is consistent with the result under simulated sunlight. Thus, CBO/CQDs has the highest photocatalytic performance under both solar and visible light irradiation. It should be noted that the contribution of visible light on ceftriaxone sodium degradation is still relatively low. Therefore, the improved photocatalytic efficiency by CBO/CQDs is predominantly promoted by charge carrier separation and migration rather than the enhanced visible light utilization.

To further confirm the reactivity of CBO/CQDs, three-dimensional excitation-emission matrix fluorescence spectroscopy (3D EEMs) were utilized to study the ceftriaxone sodium removal process and the degree of ceftriaxone sodium mineralization during the photocatalysis process. Fig. 6a shows that there were no extra signals present in the ceftriaxone sodium solution. After being irradiated for 40 min under simulated sunlight (Fig. S5a), fluorescence peaks located at E_x/E_m = 210–225/320–345 nm and E_x/E_m = 215–220/345–350 nm appeared, which can be attributed to the production of aromatic compounds; the peak strength of aromatics decreased with longer irradiation time [58]. Moreover, with the continuous degradation of ceftriaxone sodium, the fluorescence signals appeared and got stronger over time (E_x/E_m = 200–350/400–550 nm) from 40 min to 120 min, respectively, as shown in Fig. S5 and Fig. 6b. It can be speculated that ceftriaxone sodium will continue to degrade into smaller molecular fulvic-like acids (E_x/E_m = 220–250/380–550 nm) and humic acids (E_x/E_m = 250–400/380–550 nm) [65]. The results

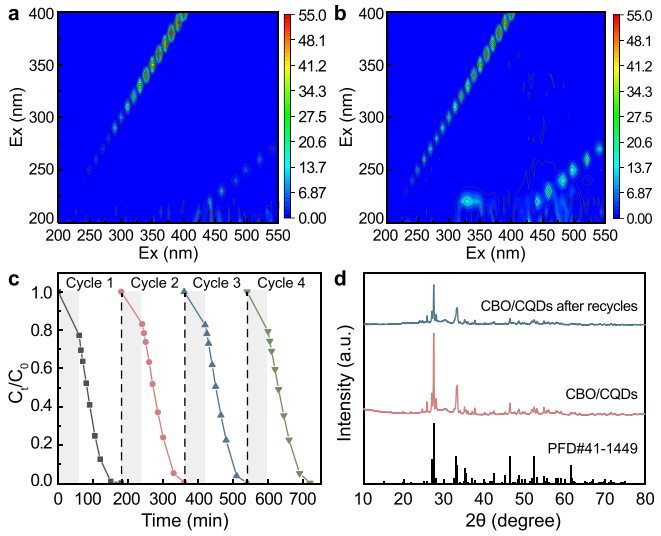

Fig. 6. **a**–**b**, 3D EEMs of ceftriaxone sodium solution after photocatalytic degradation for 0 min (**a**) and 120 min (**b**). **c**, The photocatalytic degradation of ceftriaxone sodium over CBO/CQDs in four reusing cycles. **d**, XRD patterns of fresh and used CBO/CQDs.

demonstrate that the molecular structure of ceftriaxone sodium was broken, and some intermediates were formed during photocatalytic reaction. With the increase of reaction time, the concentration of pollutants and intermediate products decreased, but the mineralization was not completed in 2 h. Fig. S6 reveals that the TOC removal efficiencies for all experiments with or without CBO/CQDs are 39.79% and 4.28%, respectively under 8 h irradiation; these results agree with the 3D EMMs data. Therefore, the ceftriaxone sodium is oxidized and forms some smaller molecules, which are hard to be further degraded. Thus, to achieve higher mineralization efficiency it is necessary either to lengthen the reaction time or increase the photocatalyst mass.

In addition, the photostability of the CBO/CQDs was evaluated by conducting ceftriaxone sodium degradation *via* reusing cycles. As shown in Fig. 6c, the CBO/CQDs sample exhibits nearly equal photocatalytic activity even after four successive reusing recycles. Meanwhile, the XRD spectra in Fig. 6d indicates no significant changes after four reusing recycles. The recycled sample was also characterized by scanning electron microscope (SEM) as shown in Fig. S7, showing that the rod-like structure was partially destructed, which could be caused by the stirring process during the degradation reaction. Therefore, the CBO/CQDs has good cyclability and a stable crystal structure.

3.4. Catalytic mechanism

The degradation of organics during the photocatalysis process is mainly caused by the reactive species (e.g., h^+, •OH, $^1O_2$, and $•O_2^-$) generated in the photocatalytic reaction. Therefore, radical trapping experiments were performed to identify the contribution of various reactive species on ceftriaxone sodium degradation. Four quenchers (TBA, AO, BQ, and L-his) were applied to capture •OH, h^+, $•O_2^-$, and $^1O_2$, respectively. The addition of TBA, AO, BQ, and L-his display suppression effects on the degradation of ceftriaxone sodium by CBO/CQDs, and the inhibitory effect order was BQ > AO > L-his > TBA (Fig. 7a). Therefore, the $•O_2^-$ and h^+ exhibited major roles on ceftriaxone sodium degradation, whereas •OH and $^1O_2$ only slightly impacted the photodegradation.

Given that $•O_2^-$ is the dominant reactive species in the ceftriaxone sodium photodegradation, NBT was used as $•O_2^-$ probe to capture the formed $•O_2^-$ to further elucidate the photocatalytic production of $•O_2^-$. The $•O_2^-$ can react with NBT to generate formazan precipitate, and the concentration of the generated $•O_2^-$ can be determined by monitoring the consumption of NBT *via* UV–vis spectrophotometry. As shown in Fig. S8, the absorbance of NBT in the photocatalysis system with BO, CBO-3, BO/EG, and CBO/CQDs gradually decreased during the reaction, indicating that all systems could produce $•O_2^-$ under solar light irradiation. In addition, the result reveals that the CBO/CQDs generates the most $•O_2^-$, with a transformation efficiency rate of 37.60%, which is favorable for the improved photocatalytic activity (Fig. 7b).

In section 3.2, the E_{CB} of BO, CBO-3, and CBO/CQDs were calculated as −0.62, −0.60, and −0.59 eV vs. NHE, respectively. The E_{VB} of BO, CBO-3, and CBO/CQDs were +2.11, +1.79, and +2.01 eV vs. NHE, respectively. The schematic band structure is proposed for the BO, CBO-3, and CBO/CQDs (as shown in Fig. 7c). The interstitial carbon changes the VB of α-Bi_2O_3, which could generate the localized states above the VB, broadening the utilization range of visible light and reducing the E_g of Bi_2O_3. Moreover, introducing localized states promotes the separation of photogenerated charge carriers, further enhancing the photocatalytic activity [28,66].

The possible photocatalytic degradation mechanism of ceftriaxone sodium over CBO/CQDs is shown in Fig. 7c. Under solar light illumination, CBO/CQDs could be stimulated to generate holes on the VB and electrons on the CB. Meanwhile, the localized states induced by carbon doping would act as a springboard for the migration of VB generated electron to the CB, thus promoting charge carriers separation and migration [50]. Moreover, the electrons excited from the VB of CBO to the CB could be collected by CQDs, thus extending the lifetime of electrons [67]. Subsequently, holes remaining in the VB or in localized states or both would be directly involved in the oxidation of ceftriaxone sodium. Thus, the surface decorated CQDs could act as electron traps to inhibit the recombination of photogenerated electrons and holes in CBO/CQDs.

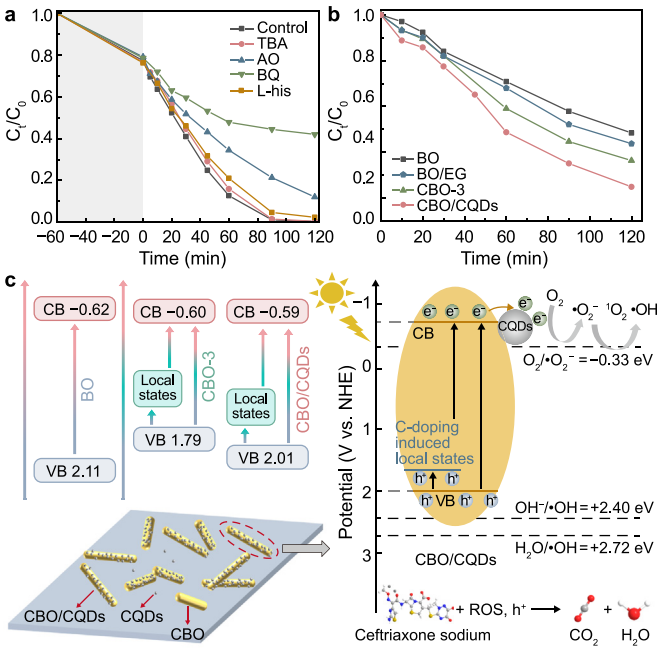

Fig. 7. **a**, Photocatalytic degradation of ceftriaxone sodium under solar light over CBO/CQDs photocatalyst with different quenchers. **b**, Photocatalytic degradation of NBT in the presence of various photocatalysts. **c**, Band edge potentials of the obtained samples, and possible photocatalytic mechanism of the CBO/CQDs under solar light irradiation.

The above PL, photocurrent, and EIS studies have demonstrated that the interstitial carbon doping and CQDs modification efficiently separate the photogenerated electrons and holes, and charge carriers transfer rate is higher than the pure BO (Fig. 4d–f). Moreover, the upconverted PL property of CQDs could enhance visible light absorption of CBO/CQDs. Accordingly, the electrons in the CB of CBO/CQDs ($E_{CB} = -0.59$ eV) could reduce O_2 to $\bullet O_2^-$ as the $E(O_2/\bullet O_2^-) = -0.33$ eV vs. NHE. However, the VB potential of CBO/CQDs (2.01 eV) is more negative than $E(\bullet OH/OH^-)$ (+2.40 eV vs. NHE) and $E(H_2O/\bullet OH)$ (+2.72 eV vs. NHE), thus the h^+ accumulated in the VB of CBO/CQDs could not oxidize OH^- or H_2O to •OH [68,69]. Therefore, the generated •OH may be originated from the reduction of $\bullet O_2^-$ (equations (6) and (8)). The above results agree with the radical trapping experiments. The photocatalytic reactions of ceftriaxone sodium are presented in equations (3)–(9).

$$\text{CBO / CQDs} + h\nu \rightarrow \text{CBO / CQDs } (e^- + h^+) \quad (3)$$

$$\text{Ceftriaxone sodium} + h^+ \rightarrow \text{Ceftriaxone sodium}^+ \rightarrow CO_2 + H_2O \quad (4)$$

$$O_2 + e^- \rightarrow \bullet O_2^- \quad (5)$$

$$\bullet O_2^- + 2H^+ + e^- \rightarrow H_2O_2 \quad (6)$$

$$2 \bullet O_2^- + 2H^+ \rightarrow {}^1O_2 + H_2O_2 \quad (7)$$

$$H_2O_2 + e^- \rightarrow OH^- + \bullet OH \quad (8)$$

$$\text{Ceftriaxone sodium} + \text{ROS} \rightarrow \text{intermediates} \rightarrow CO_2 + H_2O \quad (9)$$

The surface properties of the photocatalyst are important in promoting photocatalytic activity. The FESEM, TEM, and BET analyses show that the EG treatment decreased the size of CBO/CQDs, leading to the increase of specific surface area and reactive sites. In addition, with the CQDs modification, the specific surface area of CBO/CQDs increased, which provided this material with higher adsorption capacity. Thus, the photodegradation of ceftriaxone sodium by generated active species would be enhanced. Moreover, the smaller particle sizes favor the transfer of charge carriers to the surface of the catalyst, increasing the possibility of surface reactions [70]. Therefore, the synergistic effect of carbon doping, CQDs deposition, and reduced particle size, boosted photocatalytic activity under solar light illumination.

3.5. The photocatalytic degradation process of ceftriaxone sodium and its toxicity evolution

To reveal the photocatalytic degradation pathways of ceftriaxone sodium using CBO/CQDs, the DFT calculation and LC-MS analysis were conducted. Based on Fukui function, the DFT calculation can predict the regioselectivity of reactive species to attack the ceftriaxone sodium molecules and the formed intermediates [71]. According to the radical trapping experiments (Fig. 7a), $\bullet O_2^-$ is the dominant reactive specie in the photodegradation of ceftriaxone sodium. Therefore, the region of ceftriaxone sodium molecule with higher Fukui index (f^+ and f^0) values are susceptible to be attacked by $\bullet O_2^-$ and get electrons [72]. Table S4 clearly presents the distribution of f^+ and f^0 values on ceftriaxone sodium molecule, where the sodium is not considered as ionized into aqueous phase, and the value of hydrogen is not listed. The S16, C17, N21, N27, S30, and O36 sites with high f^+or f^0 values are more likely to be attacked by reactive species (Fig. 8a). Fig. 8b shows the electrostatic potential (ESP) map of ceftriaxone sodium molecule, the S16, C17, N21, N27, and O36 sites show positive electrostatic potential, which is easily attacked by a negatively charged reactive species (i.e., $\bullet O_2^-$).

Combined with LC-MS analysis (Table S5 and Fig. S9), the possible degradation pathways of ceftriaxone sodium are illustrated in Fig. 8c. Sodium in ceftriaxone is dissolves. It is replaced by hydrogen to form the intermediates: A, the O36 with high f^0 value (0.043875) will be attacked by $\bullet O_2^-$ to form the intermediates B. In pathway I, C17 is vulnerable to be attacked by $\bullet O_2^-$, inducing the cleavage of the C–C bond of intermediates B to form the intermediates C. Meanwhile, intermediates D, E, and F could derive from bond ruptures at the C–C or C–N and C–S bonds (labeled with dashed lines) in the B molecule [73]. In pathway II, the intermediates G and H are formed due to the loss of carbonyl group and the fracture of β-lactam from the structure of intermediate B [37]. The high f^0 value (0.04228) of S16 results in the cleavage of S–C bond of intermediate H to form intermediate I, which can be degraded to intermediates J and K. In pathway III, N21 and C17 with high f^+ values will result in the cleavage of the N–O and C–C bonds of intermediate B to form the intermediates C and L. The intermediate M will be generated due to the opening of quaternion ring and loss of small molecules from intermediate L. Finally, intermediate M is fragmented into intermediates F and N. Eventually, products C, D, E, J, K, and N, are mineralized into H_2O and CO_2.

Many intermediates can be more toxic than the target pollutants in the photocatalytic degradation processes. Therefore, the Toxicity Estimation Software Tool (T.E.S.T.) was used to evaluate the acute toxicity, developmental toxicity, bioaccumulation factor, and mutagenicity of ceftriaxone and its degradation intermediates (Fig. 9 and Table S6) [74]. The acute toxicity was evaluated by LC_{50} value, as shown in Fig. 9a, the LC_{50} of ceftriaxone was 217.26 mg L^{-1}, which can be categorized as “Not harmful”. Although the LC_{50} for most detected intermediates are lower than ceftriaxone, which are still “harmful”. One of the most abundant intermediates, the chemical I, is classified as “not harmful”. Fig. 9b shows that all intermediates have higher developmental toxicity than ceftriaxone, but most of them are labeled “developmental non-toxic”. In Fig. 9c, the bioaccumulation factor of all detected intermediates is higher than ceftriaxone, which indicates that they have higher possibility to accumulate in animal tissues. The mutagenicity of all intermediates (except F) is higher than ceftriaxone (Fig. 9d). Generally, based on the toxicity assessment, most photocatalytic degradation intermediates show higher toxicity than ceftriaxone. Therefore, to ensure water safety it is necessary to prolong the degradation time to achieve high mineralization.

4. Conclusion

A novel carbon quantum dots (CQDs) modified C-doped α-Bi_2O_3 photocatalyst (CBO/CQDs) was obtained by solvothermal reduction of doped carbon. Material characterizations revealed that CBO/CQDs has rod-like structure with slit-like pores, which are evenly loaded with CQDs. This material showed prominent photocatalytic activity for ceftriaxone sodium degradation. The k value of CBO/CQDs was 11.4 or 3.2 times that of pure α-Bi_2O_3 and CBO-3. This enhanced photocatalytic activity mainly derives from the compound effects of carbon doping, CQDs deposition, and reduced particle size: (i) The interstitial carbon doping generates the localized states above the VB, which enhances the utilization of visible light and facilitates the photogenerated electrons and holes separation. (ii) The surface decorated CQDs improves the charge carrier separation and extends the visible light response. (iii) The reduced particle size of CBO/CQDs accelerates migration of

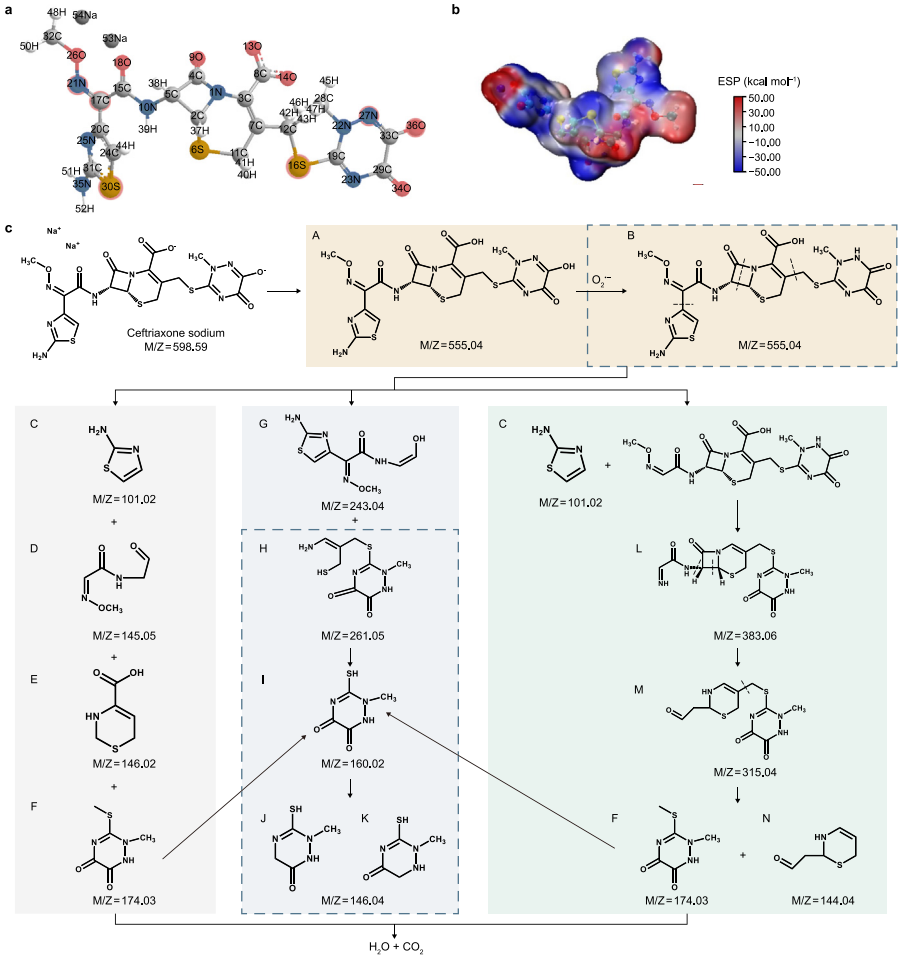

Fig. 8. **a**, Chemical structure of ceftriaxone sodium. **b**, ESP mapping of ceftriaxone sodium. **c**, The possible photodegradation pathways of ceftriaxone sodium in the CBO/CQDs photocatalysis system.

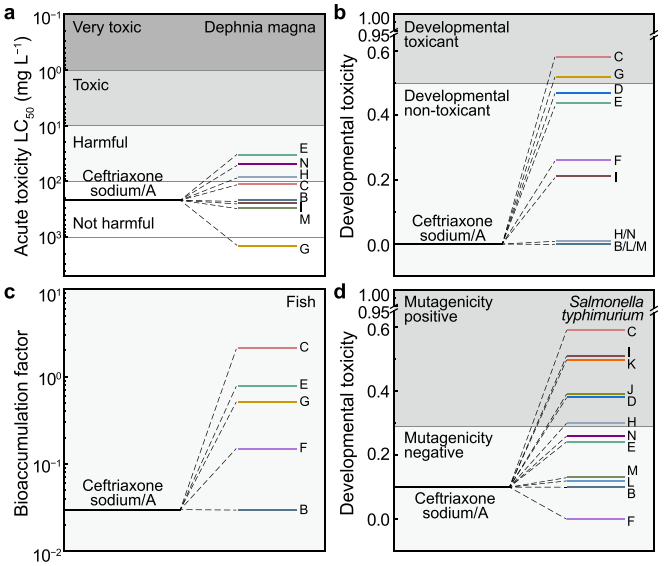

Fig. 9. Acute toxicity (**a**), developmental toxicity (**b**), bioaccumulation factor (**c**), and mutagenicity (**d**) of ceftriaxone and degradation intermediates.

photogenerated carriers. The free radical quenching experiments showed that the photogenerated $\bullet O_2^-$ was the most crucial reactive species on ceftriaxone sodium degradation. The reusing experiments proved that CBO/CQDs held good photostability. The 3D EEMs and TOC analyses revealed that longer reaction time or higher photocatalyst dosage are required to achieve sufficient mineralization. Moreover, the photocatalytic degradation pathways of ceftriaxone sodium were proposed by intermediates analysis and DFT calculation. According to the QSAR analysis, some degradation intermediates possessed high toxicity, which required sufficient mineralization to ensure safe discharge.

Declaration of comepting interest

The authors declare that they have no known competing financial interests or personal relationships that could have appeared to influence the work reported in this paper.

Acknowledgments

This study was financially supported by the National Key R&D Program (2019YFC0408200), Natural Science Foundation of Shanghai [21ZR1415600] and National Natural Science Foundation of China [41807340].

Appendix A. Supplementary data

Supplementary data to this article can be found online at https://doi.org/10.1016/j.ese.2022.100219.

References

[1] G.Y. Chen, Y. Yu, L. Liang, X.G. Duan, R. Li, X.K. Lu, B.B. Yan, N. Li, S.B. Wang, Remediation of antibiotic wastewater by coupled photocatalytic and persulfate oxidation system: a critical review, J. Hazard Mater. 408 (2021). Article 124461.

[2] Q.Q. Zhang, G.G. Ying, C.G. Pan, Y.S. Liu, J.L. Zhao, Comprehensive evaluation of antibiotics emission and fate in the river basins of China: source analysis, multimedia modeling, and linkage to bacterial resistance, Environ. Sci. Technol. 49 (11) (2015) 6772–6782.

[3] Z.Q. Cai, A.D. Dwivedi, W.N. Lee, X. Zhao, W. Liu, M. Sillanpaa, D.Y. Zhao, C.H. Huang, J. Fu, Application of nanotechnologies for removing pharmaceutically active compounds from water: development and future trends, Environ. Sci.-Nano. 5 (1) (2018) 27–47.

[4] S. Srinithi, V. Balakumar, S.M. Chen, In-situ fabrication of polypyrrole composite with MoO_3: an effective interfacial charge transfers and electrode materials for degradation and determination of acetaminophen, Chemosphere 291 (2022). Article 132977.

[5] S.L. Zheng, X.Y. Qiu, B. Chen, X.G. Yu, Z.H. Liu, G.P. Zhong, H.Y. Li, M. Chen, G.D. Sun, H. Huang, W.W. Yu, D. Freestone, Antibiotics pollution in Jiulong River estuary: source, distribution and bacterial resistance, Chemosphere 84 (11) (2011) 1677–1685.

[6] Y.Y. Zhao, X.H. Liang, Y.B. Wang, H.X. Shi, E.Z. Liu, J. Fan, X.Y. Hu, Degradation and removal of Ceftriaxone sodium in aquatic environment with Bi_2WO_6/g-C_3N_4 photocatalyst, J. Colloid Interface Sci. 523 (2018) 7–17.

[7] S.S. Liu, H.X. Zhao, H.J. Lehmler, X.Y. Cai, J.W. Chen, Antibiotic pollution in marine food webs in Laizhou Bay, North China: trophodynamics and human exposure implication, Environ. Sci. Technol. 51 (4) (2017) 2392–2400.

[8] E.S. Elmolla, M. Chaudhuri, Photocatalytic degradation of amoxicillin, ampicillin and cloxacillin antibiotics in aqueous solution using UV/TiO_2 and UV/H_2O_2/TiO_2 photocatalysis, Desalination 252 (1-3) (2010) 46–52.

[9] D. Huang, X.B. Sun, Y.D. Liu, H.D. Ji, W. Liu, C.C. Wang, W.Y. Ma, Z.Q. Cai, A carbon-rich g-C_3N_4 with promoted charge separation for highly efficient photocatalytic degradation of amoxicillin, Chin. Chem. Lett. 32 (9) (2021) 2787–2791.

[10] D.L. Huang, Z.H. Li, G.M. Zeng, C.Y. Zhou, W.J. Xue, X.M. Gong, X.L. Yan, S. Chen, W.J. Wang, M. Cheng, Megamerger in photocatalytic field: 2D g-C_3N_4 nanosheets serve as support of 0D nanomaterials for improving photocatalytic performance, Appl. Catal. B Environ. 240 (2019) 153–173.

[11] M. Cheng, G.M. Zeng, D.L. Huang, C. Lai, Y. Liu, C. Zhang, J. Wan, L. Hu, C.Y. Zhou, W.P. Xiong, Efficient degradation of sulfamethazine in simulated and real wastewater at slightly basic pH values using Co-SAM-SCS/H_2O_2 Fenton-like system, Water Res. 138 (2018) 7–18.

[12] A. Kumar, A. Kumar, V. Krishnan, Perovskite oxide based materials for energy and environment-oriented photocatalysis, ACS Catal. 10 (17) (2020) 10253–10315.

[13] D. Majhi, P.K. Samal, K. Das, S.K. Gouda, Y.P. Bhoi, B.G. Mishra, Alpha-NiS/Bi_2O_3 nanocomposites for enhanced photocatalytic degradation of tramadol, ACS Appl. Nano Mater. 2 (1) (2019) 395–407.

[14] Y. Sang, X. Cao, G.D. Dai, L.X. Wang, Y. Peng, B.Y. Geng, Facile one-pot synthesis of novel hierarchical Bi_2O_3/Bi_2S_3 nanoflower photocatalyst with intrinsic p-n junction for efficient photocatalytic removals of RhB and Cr(VI), J. Hazard Mater. 381 (2020). Article 120942.

[15] Y.Q. Cui, L.C. Nengzi, J.F. Gou, Y. Huang, B. Li, X.W. Cheng, Fabrication of dual Z-scheme MIL-53(Fe)/alpha-Bi_2O_3/g-C_3N_4 ternary composite with enhanced visible light photocatalytic performance, Separ. Purif. Technol. 232 (2020). Article 115959.

[16] H.J. Lu, Q. Hao, T. Chen, L.H. Zhang, D.M. Chen, C. Ma, W.Q. Yao, Y.F. Zhu, A high-performance Bi_2O_3/Bi_2SiO_5 p-n heterojunction photocatalyst induced by phase transition of Bi_2O_3, Appl. Catal. B Environ. 237 (2018) 59–67.

[17] J.L. Hu, H.M. Li, C.J. Huang, M. Liu, X.Q. Qiu, Enhanced photocatalytic activity of Bi_2O_3 under visible light irradiation by Cu(II) clusters modification, Appl. Catal. B Environ. 142 (2013) 598–603.

[18] W. Raza, M.M. Haque, M. Muneer, T. Harada, M. Matsumura, Synthesis, characterization and photocatalytic performance of visible light induced bismuth oxide nanoparticle, J. Alloys Compd. 648 (2015) 641–650.

[19] B.B. Shao, X.J. Liu, Z. Liu, G.M. Zeng, Q.H. Liang, C. Liang, Y. Cheng, W. Zhang, Y. Liu, S.X. Gong, A novel double Z-scheme photocatalyst Ag_3PO_4/Bi_2S_3/Bi_2O_3 with enhanced visible-light photocatalytic performance for antibiotic degradation, Chem. Eng. J. 368 (2019) 730–745.

[20] M. Faisal, A.A. Ibrahim, H. Bouzid, S.A. Al-Sayari, M.S. Al-Assiri, A.A. Ismail, Hydrothermal synthesis of Sr-doped alpha-Bi_2O_3 nanosheets as highly efficient photocatalysts under visible light, J. Mol. Catal. Chem. 387 (2014) 69–75.

[21] V. Balakumar, S. Selvarajan, A. Baishnisha, S. Kathiresan, In-situ growth of TiO_2@B-doped g-C_3N_4 core-shell nanospheres for boosts the photocatalytic detoxification of emerging pollutants with mechanistic insight, Appl. Surf. Sci. 577 (2022). Article 151924.

[22] Y.D. Luo, Q.Q. Huang, B. Li, L.H. Dong, M.G. Fan, F.Y. Zhang, Synthesis and characterization of Cu_2O modified Bi_2O_3 nanospheres with enhanced visible light photocatalytic activity, Appl. Surf. Sci. 357 (2015) 1072–1079.

[23] P. Zhang, Y. Huang, Y.F. Rao, M.J. Chen, X.W. Li, W.K. Ho, S.C. Lee, J.J. Cao, Chemical etching fabrication of uniform mesoporous Bi@Bi_2O_3 nanospheres with enhanced visible light-induced photocatalytic oxidation performance for NO_x, Chem. Eng. J. 406 (2021). Article 126910.

[24] G. Fan, Z. Ma, X. Li, L. Deng, Coupling of Bi_2O_3 nanoparticles with g-C_3N_4 for enhanced photocatalytic degradation of methylene blue, Ceram. Int. 47 (4) (2021) 5758–5766.

[25] F. Fu, H.D. Shen, W.W. Xue, Y.Z. Zhen, R.A. Soomro, X.X. Yang, D.J. Wang, B. Xu, R. Chi, Alkali-assisted synthesis of direct Z-scheme based Bi_2O_3/Bi_2MoO_6 photocatalyst for highly efficient photocatalytic degradation of phenol and hydrogen evolution reaction, J. Catal. 375 (2019) 399–409.

[26] G. Dai, S. Liu, Y. Liang, A simple preparation of carbon doped porous Bi_2O_3 with enhanced visible-light photocatalytic activity, J. Alloys Compd. 608 (2014) 44–48.

[27] W.J. Ren, Z.H. Ai, F.L. Jia, L.Z. Zhang, X.X. Fan, Z.G. Zou, Low temperature preparation and visible light photocatalytic activity of mesoporous carbon-doped crystalline TiO_2, Appl. Catal. B Environ. 69 (3-4) (2007) 138–144.

[28] T. Xiong, H.W. Huang, Y.J. Sun, F. Dong, In situ synthesis of a C-doped $(BiO)_2CO_3$ hierarchical self-assembly effectively promoting visible light photocatalysis, J. Mater. Chem. A. 3 (11) (2015) 6118–6127.

[29] L. Zeng, F. Zhe, Y. Wang, Q. Zhang, X. Zhao, X. Hu, Y. Wu, Y. He, Preparation of interstitial carbon doped BiOI for enhanced performance in photocatalytic nitrogen fixation and methyl orange degradation, J. Colloid Interface Sci. 539 (2019) 563–574.

[30] V. Balakumar, M. Ramalingam, K. Sekar, C. Chuaicham, K. Sasaki, Fabrication and characterization of carbon quantum dots decorated hollow porous graphitic carbon nitride through polyaniline for photocatalysis, Chem. Eng. J. 426 (2021). Article 131739.

[31] J.H. Lai, X.Y. Jiang, M. Zhao, S.A. Cui, J. Yang, Y.F. Li, Thickness-dependent layered $BiOIO_3$ modified with carbon quantum dots for photodegradation of bisphenol A: mechanism, pathways and DFT calculation, Appl. Catal. B Environ. 298 (2021). Article 120622.

[32] Q.H. Que, Y.L. Xing, Z.L. He, Y.W. Yang, X.T. Yin, W.X. Que, Bi_2O_3/Carbon quantum dots heterostructured photocatalysts with enhanced photocatalytic activity, Mater. Lett. 209 (2017) 220–223.

[33] T. Xian, X.F. Sun, L.J. Di, Y.J. Zhou, J. Ma, H.Q. Li, H. Yang, Carbon quantum dots (CQDs) decorated Bi_2O_{3-x} hybrid photocatalysts with promising NIR-light-driven photodegradation activity for AO7, Catalysts 9 (12) (2019). Article 1031.

[34] J. Li, L. Cai, J. Shang, Y. Yu, L. Zhang, Giant enhancement of internal electric field boosting bulk charge separation for photocatalysis, Adv. Mater. 28 (21) (2016) 4059–4064.

[35] X. Chen, X. Zhang, Y.H. Li, M.Y. Qi, J.Y. Li, Z.R. Tang, Z. Zhou, Y.J. Xu, Transition metal doping BiOBr nanosheets with oxygen vacancy and exposed {102} facets for visible light nitrogen fixation, Appl. Catal. B Environ. 281 (2021). Article 119516.

[36] R. Jiang, G. Lu, Z. Yan, D. Wu, R. Zhou, X. Bao, Insights into a CQD-$SnNb_2O_6$/BiOCl Z-scheme system for the degradation of benzocaine: influence factors, intermediate toxicity and photocatalytic mechanism, Chem. Eng. J. 374 (2019) 79–90.

[37] Y.Y. Zhao, X.H. Liang, H.X. Shi, Y.B. Wang, Y.K. Ren, E.Z. Liu, X. Zhang, J. Fan, X.Y. Hu, Photocatalytic activity enhanced by synergistic effects of nano-silver and ZnSe quantum dots co-loaded with bulk g-C_3N_4 for Ceftriaxone sodium degradation in aquatic environment, Chem. Eng. J. 353 (2018) 56–68.

[38] N. Tian, H.W. Huang, Y. He, Y.X. Guo, T.R. Zhang, Y.H. Zhang, Mediator-free direct Z-scheme photocatalytic system: $BiVO_4$/g-C_3N_4 organic-inorganic hybrid photocatalyst with highly efficient visible-light-induced photocatalytic activity, Dalton Trans. 44 (9) (2015) 4297–4307.

[39] S.N. Baker, G.A. Baker, Luminescent carbon nanodots: emergent nanolights, Angew. Chem.-Int. Edit. 49 (38) (2010) 6726–6744.

[40] A. Mahmood, G.S. Shi, Z. Wang, Z.P. Rao, W. Xiao, X.F. Xie, J. Sun, Carbon quantum dots-TiO_2 nanocomposite as an efficient photocatalyst for the photodegradation of aromatic ring-containing mixed VOCs: an experimental and DFT studies of adsorption and electronic structure of the interface, J. Hazard Mater. 401 (2021). Article 123402.

[41] Z.Q. Chen, P.X. Xing, P.F. Chen, Q.Q. Chen, Y. Wang, J.X. Yu, Y.M. He, Synthesis of carbon doped $KTaO_3$ and its enhanced performance in photocatalytic H_2 generation, Catal. Commun. 109 (2018) 6–9.

[42] V.N. Denisov, A.N. Ivlev, A.S. Lipin, B.N. Mavrin, V.G. Orlov, Raman spectra and lattice dynamics of single-crystal alpha-Bi_2O_3, J. Phys.-Condes. Matter. 9 (23) (1997) 4967–4978.

[43] M. Malligavathy, S. Iyyapushpam, S.T. Nishanthi, D.P. Padiyan, Remarkable catalytic activity of Bi_2O_3/TiO_2 nanocomposites prepared by hydrothermal method for the degradation of methyl orange, J. Nanoparticle Res. 19 (4) (2017). Article 144.

[44] J. Sun, H. Xu, D. Li, Z. Zou, Q. Wu, G. Liu, J. Yang, L. Sun, D. Xia, Ultrasound-assisted synthesis of a feathery-shaped BiOCl with abundant oxygen vacancies and efficient visible-light photoactivity, New J. Chem. 42 (24) (2018) 19571–19577.

[45] W. Chen, T.Y. Liu, T. Huang, X.H. Liu, X.J. Yang, Novel mesoporous P-doped graphitic carbon nitride nanosheets coupled with $ZnIn_2S_4$ nanosheets as efficient visible light driven heterostructures with remarkably enhanced photo-reduction activity, Nanoscale 8 (6) (2016) 3711–3719.

[46] H. Huang, X. Li, J. Wang, F. Dong, P.K. Chu, T. Zhang, Y. Zhang, Anionic group self-doping as a promising strategy: band-gap engineering and multi-functional applications of high-performance CO_3^{2-}-doped $Bi_2O_2CO_3$, ACS Catal. 5 (7) (2015) 4094–4103.
[47] Y. Sun, C.J. Murphy, K.R. Reyes-Gil, E.A. Reyes-Garcia, J.M. Thornton, N.A. Morris, D. Raftery, Photoelectrochemical and structural characterization of carbon-doped WO_3 films prepared via spray pyrolysis, Int. J. Hydrogen Energy 34 (20) (2009) 8476–8484.
[48] Y.X. Xing, X.C. Gao, G.F. Ji, Z.L. Liu, C.F. Du, Synthesis of carbon doped Bi_2MoO_6 for enhanced photocatalytic performance and tumor photodynamic therapy efficiency, Appl. Surf. Sci. 465 (2019) 369–382.
[49] H.Y. Li, D.J. Wang, H.M. Fan, P. Wang, T.F. Jiang, T.F. Xie, Synthesis of highly efficient C-doped TiO_2 photocatalyst and its photo-generated charge-transfer properties, J. Colloid Interface Sci. 354 (1) (2011) 175–180.
[50] X.L. Jin, C.D. Lv, X. Zhou, C.M. Zhang, B. Zhang, H. Su, G. Chen, Realizing the regulated carrier separation and exciton generation of $Bi_{24}O_{31}Cl_{10}$ via a carbon doping strategy, J. Mater. Chem. A. 6 (47) (2018) 24350–24357.
[51] J.X. Xia, J. Di, H.T. Li, H. Xu, H.M. Li, S.J. Guo, Ionic liquid-induced strategy for carbon quantum dots/BiOX (X=Br, Cl) hybrid nanosheets with superior visible light-driven photocatalysis, Appl. Catal. B Environ. 181 (2016) 260–269.
[52] L.B. Jiang, X.Z. Yuan, G.M. Zeng, J. Liang, X.H. Chen, H.B. Yu, H. Wang, Z.B. Wu, J. Zhang, T. Xiong, In-situ synthesis of direct solid-state dual Z-scheme WO_3/g-C_3N_4/Bi_2O_3 photocatalyst for the degradation of refractory pollutant, Appl. Catal. B Environ. 227 (2018) 376–385.
[53] Y. Sun, C.J. Murphy, K.R. Reyes-Gil, E.A. Reyes-Garcia, J.P. Lilly, D. Raftery, Carbon-doped In_2O_3 films for photoelectrochemical hydrogen production, Int. J. Hydrogen Energy 33 (21) (2008) 5967–5974.
[54] Z.G. Xiong, X.S. Zhao, Nitrogen-doped titanate-anatase core-shell nanobelts with exposed {101} anatase facets and enhanced visible light photocatalytic activity, J. Am. Chem. Soc. 134 (13) (2012) 5754–5757.
[55] Y. Liang, W.C. Xu, J.Z. Fang, Z. Liu, D.D. Chen, T. Pan, Y.T. Yu, Z.Q. Fang, Highly dispersed bismuth oxide quantum dots/graphite carbon nitride nanosheets heterojunctions for visible light photocatalytic redox degradation of environmental pollutants, Appl. Catal. B Environ. 295 (2021). Article 120279.
[56] W.Y. Dou, X.Y. Hu, L.H. Kong, X.J. Peng, Photo-induced dissolution of Bi_2O_3 during photocatalysis reactions: mechanisms and inhibition method, J. Hazard Mater. 412 (2021). Article 125267.
[57] C. Zeng, Y. Hu, H. Huang, $BiOBr_{0.75}I_{0.25}$/$BiOIO_3$ as a novel heterojunctional photocatalyst with superior visible-light-driven photocatalytic activity in removing diverse industrial pollutants, ACS Sustain. Chem. Eng. 5 (5) (2017) 3897–3905.
[58] W. Xue, D. Huang, J. Li, G. Zeng, R. Deng, Y. Yang, S. Chen, Z. Li, X. Gong, B. Li, Assembly of AgI nanoparticles and ultrathin g-C_3N_4 nanosheets codecorated Bi_2WO_6 direct dual Z-scheme photocatalyst: an efficient, sustainable and heterogeneous catalyst with enhanced photocatalytic performance, Chem. Eng. J. 373 (2019) 1144–1157.
[59] X. Qi, H.J. Zhang, Y.Q. Li, J.H. Chen, Density functional theory study of the structure and properties of C-doped pyrite, Physica B 572 (2019) 168–174.
[60] C.Q. Li, X.B. Dong, N.Y. Zhu, X.W. Zhang, S.S. Yang, Z.M. Sun, Y.Y. Liu, S.L. Zheng, D.D. Dionysiou, Rational design of efficient visible-light driven photocatalyst through 0D/2D structural assembly: Natural kaolinite supported monodispersed TiO_2 with carbon regulation, Chem. Eng. J. 396 (2020). Article 125311.
[61] Y. Wang, W. Jiang, W. Luo, X. Chen, Y. Zhu, Ultrathin nanosheets g-C_3N_4@Bi_2WO_6 core-shell structure via low temperature reassembled strategy to promote photocatalytic activity, Appl. Catal. B Environ. 237 (2018) 633–640.
[62] Y. Tian, N. Jia, H. Ma, G. Liu, Z. Xiao, Y. Wu, L. Zhou, J. Lei, L. Wang, Y. Liu, J. Zhang. 0D/3D coupling of g-C_3N_4 QDs/hierarchical macro-mesoporous CuO-SiO_2 for high-efficiency norfloxacin removal in photo-Fenton-like processes, J. Hazard Mater. 419 (2021). Article 126359.
[63] X.J. Wen, C.G. Niu, H. Guo, L. Zhang, C. Liang, G.M. Zeng, Photocatalytic degradation of levofloxacin by ternary Ag_2CO_3/CeO_2/AgBr photocatalyst under visible-light irradiation: degradation pathways, mineralization ability, and an accelerated interfacial charge transfer process study, J. Catal. 358 (2018) 211–223.
[64] F.L. Wang, Y.F. Wang, Y.P. Feng, Y.Q. Zeng, Z.J. Xie, Q.X. Zhang, Y.H. Su, P. Chen, Y. Liu, K. Yao, W.Y. Lv, G.G. Liu, Novel ternary photocatalyst of single atom-dispersed silver and carbon quantum dots co-loaded with ultrathin g-C_3N_4 for broad spectrum photocatalytic degradation of naproxen, Appl. Catal. B Environ. 221 (2018) 510–520.
[65] W. Chen, P. Westerhoff, J.A. Leenheer, K. Booksh, Fluorescence excitation - emission matrix regional integration to quantify spectra for dissolved organic matter, Environ. Sci. Technol. 37 (24) (2003) 5701–5710.
[66] J.X. Yu, Z.G. Chen, L. Zeng, Y.Y. Ma, Z. Feng, Y. Wu, H.J. Lin, L.H. Zhao, Y.M. He, Synthesis of carbon-doped $KNbO_3$ photocatalyst with excellent performance for photocatalytic hydrogen production, Sol. Energy Mater. Sol. Cells 179 (2018) 45–56.
[67] W.X. Li, Z.Z. Wang, Y. Li, J.B. Ghasemi, J. Li, G.K. Zhang, Visible-NIR light-responsive 0D/2D CQDs/Sb_2WO_6 nanosheets with enhanced photocatalytic degradation performance of RhB: unveiling the dual roles of CQDs and mechanism study, J. Hazard Mater. 424 (2022). Article 127595.
[68] B.B. Shao, Z.F. Liu, G.M. Zeng, Y. Liu, X. Yang, C.Y. Zhou, M. Chen, Y.J. Liu, Y.L. Jiang, M. Yan, Immobilization of laccase on hollow mesoporous carbon nanospheres: noteworthy immobilization, excellent stability and efficacious for antibiotic contaminants removal, J. Hazard Mater. 362 (2019) 318–326.
[69] D.L. Huang, X.L. Yan, M. Yan, G.M. Zeng, C.Y. Zhou, J. Wan, M. Cheng, W.J. Xue, Graphitic carbon nitride-based heterojunction photoactive nanocomposites: applications and mechanism insight, ACS Appl. Mater. Interfaces 10 (25) (2018) 21035–21055.
[70] H. Tong, S.X. Ouyang, Y.P. Bi, N. Umezawa, M. Oshikiri, J.H. Ye, Nano-photocatalytic materials: possibilities and challenges, Adv. Mater. 24 (2) (2012) 229–251.
[71] R.S. Rodriguez, V.M. Szlag, T.M. Reineke, C.L. Haynes, Multiplex surface-enhanced Raman scattering detection of deoxynivalenol and ochratoxin A with a linear polymer affinity agent, Mater. Adv. 1 (9) (2020) 3256–3266.
[72] Z. Cai, Y. Song, X. Jin, C.C. Wang, H. Ji, W. Liu, X. Sun, Highly efficient AgBr/h-MoO_3 with charge separation tuning for photocatalytic degradation of trimethoprim: mechanism insight and toxicity assessment, Sci. Total Environ. 781 (2021). Article 146754.
[73] Y. Zheng, X.F. Hu, F. Deng, J. Li, D.D. Dionysiou, X.B. Luo, Enhanced photocatalytic oxidizing ability of $Zn_{1-x}In_{2x/3}S$ solid solution via band structure by composition regulation, Separ. Purif. Technol. 255 (2021). Article 117726.
[74] Z.Q. Cai, X.D. Hao, X.B. Sun, P.H. Du, W. Liu, J. Fu, Highly active WO_3@anatase-SiO_2 aerogel for solar-light-driven phenanthrene degradation: mechanism insight and toxicity assessment, Water Res. 162 (2019) 369–382.